Int. J. Electrochem. Sci., 17 **(2022)** Article Number: 220939, doi: 10.20964/2022.09.40

International Journal of
ELECTROCHEMICAL
SCIENCE
www.electrochemsci.org

Growth Mechanism of Ni-graphene Composite Coating on Mild Steel: A Combined Experimental and Molecular Dynamics Study

Ruiyu Zhang[1,2], *Xiao Xing*[1,2], *Jianguo Liu*[1,2], *Gan Cui*[1,2,*], *Zili Li*[1,2,*]

[1] College of Pipeline and Civil Engineering in China University of Petroleum (East China), No. 66, West Changjiang Road, Qingdao 266580, China.
[2] Shandong Key Laboratory of Oil & Gas Storage and Transportation Safety, Qingdao 266580, China.
[*]E-mail: chennacuigan@163.com, zilimenhuzu@163.com

Received: 4 May 2022 / *Accepted:* 26 June 2022 / *Published:* 7 August 2022

In this work, experimental studies were combined with molecular dynamics (MD) simulations to obtain a better understanding of the growth process of Ni-graphene composite coating. Conventional electrochemical techniques (cyclic voltammetry and chronoamperometry) were employed to investigate the electrochemical kinetics and nucleation process of the deposition. The three-dimensional (3D) morphologies of the deposits were observed by using an atomic force microscope (AFM), and the quantitative comparison of surface parameters and grain distribution was conducted. Moreover, MD simulations were employed to model the deposition process of Ni-graphene composite coating, which revealed the co-deposition process and facilitated the prediction of surface roughness evolution. The findings reveal that the Ni-graphene electrodeposition under present conditions tends to follow instantaneous nucleation and diffusion-controlled 3D growth at the initial stage. The graphene reinforced composite coatings have higher grain density, finer grain size, and rougher surface morphology than the pure Ni coating. Enhanced electrolytic corrosion resistance and uniform graphene configuration can be achieved at an optimal graphene oxide concentration. Through systematic experimental tests and MD simulations, this work provides deeper insight into the complex deposition process of Ni-graphene composite coating.

Keywords: Nucleation, Ni-graphene, Molecular dynamics, Electrodeposition

1. INTRODUCTION

Metallic composite coatings reinforced by nanoparticles or nanoplates are of great interest to researchers in varied fields, including corrosion control, wear protection, fuel cells, etc. [1]. Due to the easy control of parameters, such as potential, temperature, and pH, electrodeposition is advantageous for the fabrication of uniform coatings and complex structures. Graphene, a two-dimensional carbon

allotrope, possesses unique two-dimensional nanostructure and superior physicochemical properties, such as gas impermeability, chemical resistance, thermal stability, and excellent mechanical properties. Moreover, graphene oxide (GO) possesses almost all the key properties of graphene and dispersibility in aqueous electrolyte due to its oxygen-containing functional groups. Therefore, graphene and its derivatives have been extensively used as the second phase to manipulate coating microstructure and enhance the properties of conventional materials.

Currently, many research works focus on the preparation process of novel coatings and the versatility of graphene in the modulation of physicochemical properties. To satisfy the demands for novel materials with specific properties and functionalities, researchers have started to synthesize nanocrystalline, functional graded, and inhomogeneous coatings with designed inner architecture [2, 3]., The coating performance fundamentally depends on the evolution of surface morphology and microstructures [4]. Thus, understanding the growth mechanism is critical for the controllable synthesis of functional films. However, the exploration of growth behavior is relatively limited. Furthermore, the growth process in graphene-added deposition involves complex dynamic processes, electrode surface properties, and co-deposition behavior. At present, the understanding of the role of graphene in the deposition process and its effect on the metal matrix is still limited.

Experimentally, the electrochemical test is an effective method to study the composite electrodeposition process. Important interface parameters can be obtained through cyclic voltammetry and chronoamperometry to provide clarity on the early-stage nucleation process. Generally, the data obtained by electrochemical technology only reflect the "averaged" state of the electrode surface, which provides a limited interpretation of the mechanisms at the atomic or nano-scale [3, 5]. Concurrently, achieving the real-time imaging of the surface during the deposition process is still a great challenge. Very few studies have observed the deposition process using advanced characterization methods, including in-situ transmission electron microscopy (TEM) [6, 7], atomic force microscopy (AFM) [8], and scanning probe microscopy [9]. Nevertheless, most studies were conducted by ex-situ investigation using scanning electron microscopy (SEM), X-ray diffraction (XRD), TEM, etc. Further exploration of the electrodeposition mechanism still requires detailed insights into the electrochemical interface.

Molecular dynamics (MD) simulation is a viable tool for understanding film growth from the nanoscale, which allows one to capture the process dynamically and build bridges between the atomic structure and macroscopic performance. In addition, as a flexible two-dimensional material, graphene usually exhibits three-dimensional characteristics as well, such as wrinkling, folding, and bending [10]. Currently, the graphene-imbedded MD models are built mainly by directly constructing bulk materials with graphene placed horizontally in the matrix [11] or treating graphene as rigid nanoplates in the deposition process. These simplified treatments ignore the randomness of graphene dispersion, the corresponding change in coating matrix, and the flexibility of the nanosheets. Therefore, the essential influence of graphene on deposition behavior and morphology evolution needs to be further explored.

This work combines experimental investigation and MD simulation to study the growth process of Ni-graphene composite coating on mild steel at the initial stage. For a deeper understanding, the nucleation mode and co-deposition behavior were studied at multiple scales. The electrodeposition mechanism of Ni-graphene composite coating can provide a theoretical basis for the design and controllable preparation of functional nanocomposite coatings.

2. EXPERIMENT

2.1 Plating bath

The composition of the plating bath is shown in Table 1. To ensure electrolyte stability, GO was selected as the starting material to construct the Ni-graphene composite coating. GO was synthesized using a modified Hummer's method [12, 13], and the procedures and characterizations are reported in detail in our previous work [2]. The as-prepared GO was mostly few-layered GO (not more than seven layers), which can be effectively reduced during the electrodeposition process [2]. Moreover, Zhang et al. [14] reported that the non-ionic surfactant polyethylene glycol (PEG) can achieve the optimal GO dispersion compared with sodium dodecyl sulfate (anionic surfactant) and cetyltrimethylammonium bromide (cationic surfactant). Thus, PEG was selected as the surfactant to disperse GO herein. The pH of the plating bath was maintained at 4.0±0.1 by using diluted hydrochloric acid and sodium hydroxide solution. Before the electrochemical tests, the plating bath was sonicated and stirred for 30 min to obtain a stable dispersion.

Table 1 Chemical composition of the plating baths.

Component	Concentration ($g \cdot L^{-1}$)
$NiCl_2$ $6H_2O$	238
H_3BO_3	31
$C_5H_{14}ClNO$	168
Graphene oxide	0, 0.05, 0.1, 0.2, 0.3
PEG (with a molecular weight of *ca*. 2000)	0.2

2.2 Characterization

Cyclic voltammetry and chronoamperometry were conducted with a PARSTAT 2273 electrochemical workstation. The electrochemical procedures were carried out in a standard three-electrode system by using a saturated calomel electrode (SCE) and platinum plate as reference electrode and counter electrode, respectively. A 1 cm^2 mild steel (20# steel) plate or glassy carbon electrode (GCE) of 3 mm diameter was used as the working electrode according to the specific test. A Luggin capillary was used to reduce solution resistance. All the electrochemical tests were conducted in the plating bath at 60±1℃ at a stirring speed of 150 $r \cdot min^{-1}$. The cyclic voltammetry (CV) test used GCE as the working electrode. The GCE was mirror-polished with 0.3 mm alumina slurry before the CV test. The potential was swept between –1.4 V and 0 V at a scan rate of 30 $mV \cdot s^{-1}$. In the chronoamperometry test, the mild steel plate was encapsulated by epoxy resin and gradually polished with 2000# SiC paper. Pre-treated mild steel was employed as the working electrode, and current time transients were recorded at varied potentials for 30 s. Unless specified, all potentials in this work were referred to the SCE.

The three-dimensional surface morphology of deposits at the early stage was observed using AFM (Park NX10, Korea) under non-contact mode. Three segregated regions (1 μm×1 μm, 256

pixels×256 pixels) in each specimen were detected. The AFM profiles were processed by XEI (Park Systems, Korea) and Mountains® software (Digital Surf, France).

3. MODEL AND METHOD

The MD simulations were conducted by the Large-scale Atomic/Molecular Massively Parallel Simulator (LAMMPS) [15, 16] and visualized by the Open Visualization Tool (OVITO) [17, 18].

As depicted in Fig.1a, the deposition process of pure metal ions mainly consists of four steps. (i) Under the action of electric field and mechanical stirring, metal ions migrate to the electric double layer through convection and diffusion. (ii) The ions undergo charge transfer across the double layer. (iii) Electrochemical reactions take place. (iv) Finally, the deposited ions diffuse to the active site and crystallize [19, 20]. Based on the deposition principle, the MD model in Fig. 1d, consisting of a substrate, adatoms, deposited atoms, graphene flakes, and solvent particles, was built to simulate the deposition process.

The dimensions of this model are 20 a×20 a×30 a, where a is the lattice parameter of Ni (approximately 70×70×106 Å). Periodic boundary conditions (PBC) were applied to the x and y directions to mimic the semi-infinite surface, while the z-direction adopted the nonperiodic boundary condition. The polycrystalline Fe substrate was created by Atomsk software using the Voronoi tessellation method [21]. As shown in Fig. 1b, the substrate contains four polycrystalline grains, where blue atoms are arranged in the body-centered cubic (BCC) lattice structure, and the grey ones represent atoms at grain boundaries. There are many active sites such as platform, step, kink, and grain boundary [22], which is consistent with the TSK (Terrace-Step-Kink) surface model proposed by Zhang et al. [23]. The bottom atoms with z-coordinate below 10 Å were not time-integrated and fixed still. The upper space of the model contained the electrolyte. To simplify the model and improve the calculation efficiency, water molecules were simplified into coarse-grained solvent particles to simulate the liquid environment [24]. A reflective wall was set on the top of the model to prevent the evaporation of the plating solution.

The electrodeposition process was simplified by adding Ni atoms and graphene flakes at a fixed frequency. The adatoms and graphene nanosheets were randomly introduced to the simulation cell from the insertion plane and electrolyte zone, respectively. To mimic the electrodeposition behavior under constant current density, the velocity of adatoms in the z-direction was kept constant, while the velocity components in the x and y directions were unconstrained. The adatoms adopted the microcanonical NVE ensemble. When the depositing atom reached within 3 Å of the electrode surface, it was assumed that it entered the electric double layer [25, 26] and 1 eV activation energy was applied to the reduced metal atom [27]. Sustainably, the atoms reached the substrate surface and found their final position after surface diffusion. Then, the atom was classified as a deposited atom and transformed into the NVT ensemble. Other atoms, including time-integrated Fe, deposited Ni, graphene flakes, and solvent particles, adopted NVT ensemble, and their temperatures were maintained through the Nose-Hoover method.

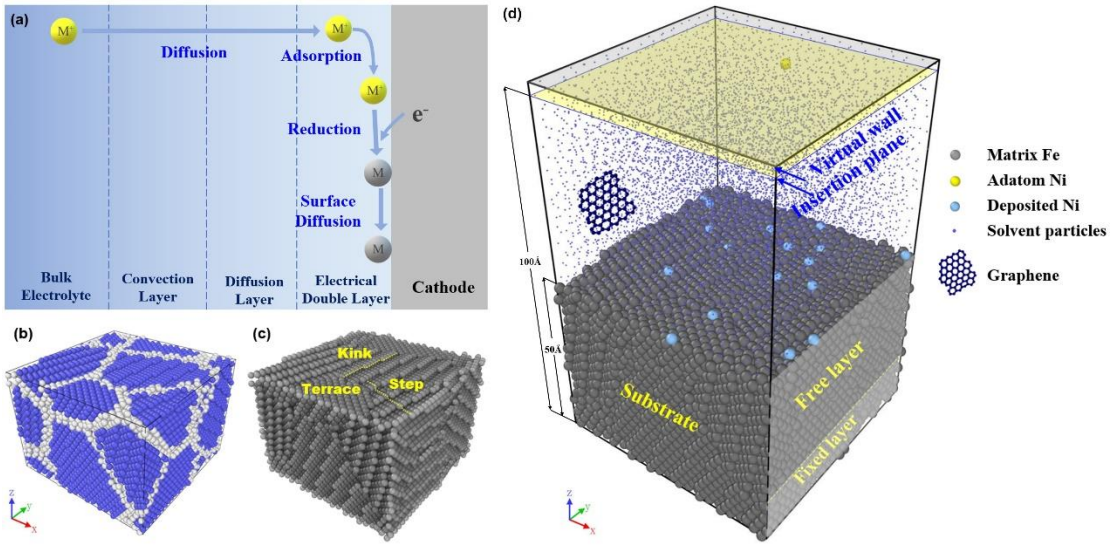

Figure 1. Schematic of the electrodeposition principle and MD model of electrodeposition. (a) Electrodeposition principle, (b) substrate grain distribution, (c) substrate surface structure, (d) MD model.

To describe the behavior of the deposition process, Table 2 specifies the interactions among atoms. The current implementation invoked the hybrid pair style in LAMMPS for using multiple potentials, including embedded-atom method (EAM) potential, adaptive intermolecular reactive empirical bond order (AIREBO) potential, Morse potential, and 12-6 Lennard-Jones (LJ) potential.

Table 2. Interatomic potentials for the Ni-graphene electrodeposition.

Pair of atoms	Type	Parameters
Fe, Ni	EAM	Developed by Bonny et al. [28, 29].
C	AIREBO	Cutoff distance=2.0 Å [30, 31].
Ni, C	Morse	β=1.8706 Å^{-1}, ε=2.4637 eV, ρ=1.7628 Å, cutoff distance=2.5 Å [32, 33].
solvent particles	LJ	ε=0.0067 eV, σ=3.1656 Å, cutoff distance=10 Å [34].
others	LJ	Calculated by Lorentz-Berthelot mixing rule (Eq. 1-2) with cutoff distance=10 Å [35].
		$\sigma_{ij} = \frac{\sigma_{ii} + \sigma_{jj}}{2}$ (1)
		$\varepsilon_{ij} = \sqrt{\varepsilon_{ii}\varepsilon_{jj}}$ (2)

The graphene nanosheet built in this work contained 35 carbon atoms. According to the published experimental works, the carbon content of graphene-based composite coatings ranges from about 14 at.% to 40 at.% [36, 37]. Thus, the simulation conditions listed in Table 3 were devised, and corresponding results were henceforth addressed as the condition name.

Table 3. MD simulation conditions for pure Ni and Ni-graphene coatings.

Simulated conditions	Number of graphene sheets	Carbon content (at.%)
Pure Ni	0	0
Ni-Gr-20	20	12.28
Ni-Gr-40	40	21.88
Ni-Gr-60	60	29.58
Ni-Gr-80	80	35.90
Ni-Gr-100	100	41.18

The system undergoes energy minimization and relaxation at 333.15 K (equals 60 ℃, the deposition temperature used in experiments) with a canonical NVT ensemble for 50 ps to obtain a stable structure before deposition. Every coating contains 5000 Ni atoms, and the total number of atoms in the model exceeds 34000. The time step was set as 1 fs, and all electrodeposition processes lasted for 25 ns. Notably, researchers have confirmed the validity of MD simulations for depicting the microstructure evolution in the deposition process, though MD simulations are conducted at an extremely short time scale (picoseconds to nanoseconds) [38].

4. RESULTS AND DISCUSSION

4.1 Nucleation process of Ni-graphene composite coating

4.1.1 Cyclic voltammetry

The voltammograms of pure Ni and Ni-graphene coatings shown in Fig. 2 exhibited a similar shape profile. The current density of pure Ni and Ni-graphene composite deposition on GCE turned negative at –0.793 V and –0.856 V, respectively. The rapid increase in negatively-charged current density indicates the fast reduction on the electrode interface and the rapid growth of the deposit. Ni^{2+} started to reduce at these initial potentials. The crystallization overpotential on 20# steel should be lower than that on GCE, because epitaxial growth cannot occur on the amorphous GCE. When the potential was further scanned to approximately –1.1 V, the increasing trend of cathode current density slowed down due to the side reactions and the formation of intermediate products [39, 40]. The reactions occurring at more negative potentials would be dominated by hydrogen evolution. With the addition of graphene, the initial deposition potential shifted negatively, indicating that the addition of graphene strengthened the cathodic polarization and inhibited the deposition process of Ni^{2+}. This phenomenon may be due to the hindered Ni^{2+} diffusion and increased solution polarization resistance caused by graphene addition. Moreover, the high conductivity and specific surface area of graphene could increase the effective area of the cathode surface and the current density.

A “nucleation loop” was formed by the intersection of forward and reverse curves, which confirmed the nucleation during the cathodic process. In the negative scan process of the CV test, the overpotential led to the reduction and nucleation, while there was no nucleation behavior during the

reverse scan process. Thus, the current density value in the positive scan was larger, and the plot during the anodic section crossed over the plot of the cathodic cycle. When the potential was subjected to the reverse scan, there was an anodic peak related to the dissolution of the deposits, as shown in inset plots in Fig. 2. The presence of graphene decreased the anodic peak current density from 0.024 $A \cdot cm^{-2}$ to 0.016 $A \cdot cm^{-2}$, indicating that graphene nanosheets can confer the coating with electrolytic corrosion resistance.

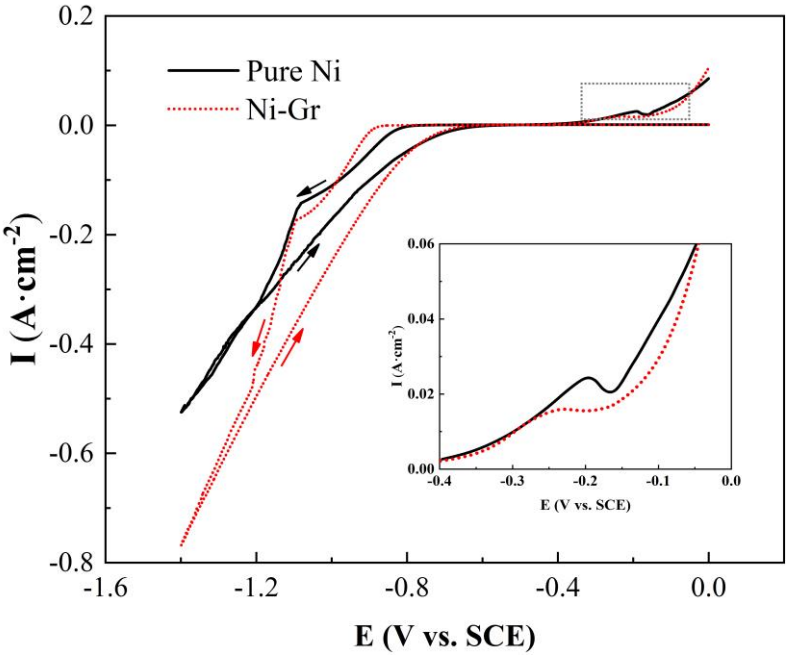

Figure 2. Cyclic voltammograms of GCE in pure Ni plating solution and Ni-graphene plating solution containing graphene oxide concentration of 0.20 $g \cdot L^{-1}$.

The cyclic voltammograms in Fig. 3 show the reduction of Ni-graphene at varied GO concentrations. To evaluate the effect of GO concentration on the deposition process, the kinetic parameters derived from the cyclic voltammograms are summarized in Table 4. With the increase in GO concentration in the plating solution, the initial deposition potential gradually shifted positively, implying that the cathodic polarization caused by graphene embedding gradually weakened. The anodic oxidation peak current density of the Ni-graphene deposit was lower than that of the pure Ni deposit when the graphene concentration was low (0.05~0.20 $g \cdot L^{-1}$). In contrast, for higher GO concentration (0.30 $g \cdot L^{-1}$), the electrolytic corrosion resistance of the deposits deteriorated, indicating that higher GO concentration did not necessarily lead to better coating performance. Hence, an optimal graphene content existed for the preparation of Ni-graphene composite coatings, which was also verified by many experimental studies [41, 42].

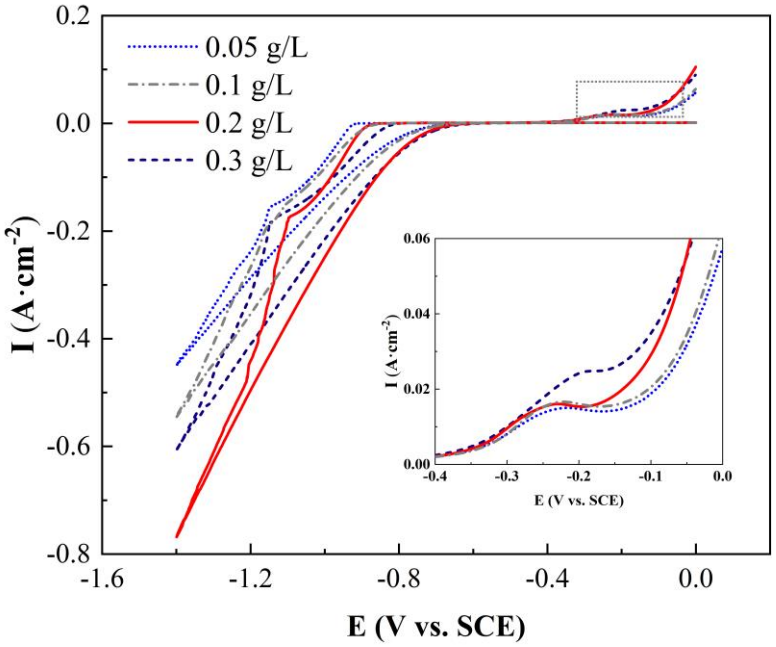

Figure 3. Cyclic voltammograms of GCE in Ni-graphene plating solution containing different graphene oxide concentrations.

Table 4. Initial deposition potential and anodic peak current density of Ni-graphene composite coating containing different graphene oxide concentrations.

GO concentration ($g \cdot L^{-1}$)	Initial deposition potential (V)	Anodic peak current density ($A \cdot cm^{-2}$)
Pure Ni coating	–0.793	0.024
0.05	–0.918	0.015
0.10	–0.858	0.017
0.20	–0.856	0.016
0.30	–0.798	0.025

4.1.2 Chronoamperometry

Chronoamperometry tests were applied to study the nucleation mechanism of the deposits at the initial stage. The *j-t* curves of pure Ni and Ni-graphene deposition recorded at different potentials exhibited the same trend (Fig. 4). In the initial period (t<1 s), current density decreased due to electrical double layer charging or adsorption processes [43]. After the induction period, the current density rose rapidly to the maximum value (i_m), due to the growth of the crystal nuclei and overlapping of the diffusion zones. The time corresponding to i_m is the nucleation relaxation time t_m. Then, the deposition process was diffusion-controlled due to the deficiency of electroactive substances. Subsequently, the current density slowly decayed and approached a stable value. All curves exhibited the typical characteristics of three-dimensional nucleation on a heterogeneous interface.

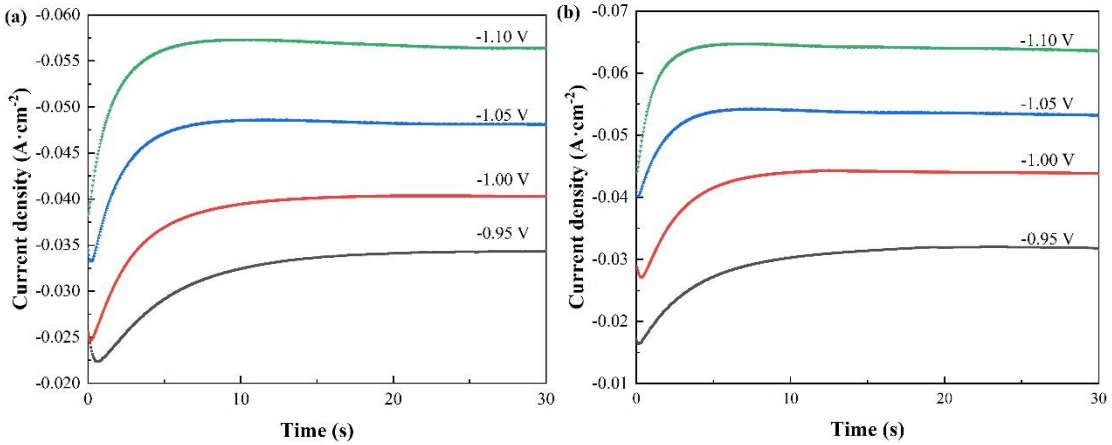

Figure 4. Chronoamperometric deposition of (a) pure Ni coating and (b) Ni-graphene composite coating on mild steel at different potentials.

The peak current density and corresponding time of pure Ni and Ni-graphene electrodeposition at different deposition potentials are provided in Table 5. The cathodic overpotential and nucleation driving force increased with the negative shift of applied potential. Thus, the peak current density increased, and the corresponding time was shortened. When the same deposition potential was applied, the i_m of Ni-graphene electrodeposition was higher, and the t_m was shorter than that of pure Ni electrodeposition. The results indicate that the addition of graphene promoted nucleation, which may be attributed to two aspects. First, graphene can induce heterogeneous nucleation by adsorbing metal ions and increasing the active surface area. Second, the conductivity of graphene can promote electrochemical reduction, increase the peak current density, and consequently accelerate the nucleation rate.

Table 5. The i_m and t_m of pure Ni and Ni-graphene deposition at different potentials.

Deposition potential (V)	Ni		Ni-Gr	
	t_m (s)	i_m (mA·cm^{-2})	t_m (s)	i_m (mA·cm^{-2})
–0.95	26.45	34.30	23.20	32.50
–1.00	20.8	40.34	12.50	44.29
–1.05	10.95	48.53	7.20	54.12
–1.10	9.85	57.32	6.65	64.75

The Scharifker–Hills model for 3D diffusion-limited nucleation in the non-dimensional form follows Eq. (3-4) [44].

Instantaneous nucleation: $$(\frac{i}{i_m})^2 = \frac{1.9542}{t/t_m}\{1-\exp[-1.2564(\frac{t}{t_m})]\}^2 \quad (3)$$

Progressive nucleation: $$(\frac{i}{i_m})^2 = \frac{1.2254}{t/t_m}\{1-\exp[-2.3367(\frac{t}{t_m})^2]\}^2 \quad (4)$$

In accordance with CV analyses, the deposition potential was set as –1.0 V. The corresponding non-dimensional plots calculated from the experimental current-time data at –1.0 V were compared with the Scharifker–Hills model. As depicted in Fig. 5, the non-dimensional $(i/i_m)^2$~(t/t_m) plots were close to the instantaneous-nucleation curves, suggesting that pure Ni and Ni-Gr deposition both followed the three-dimensional instantaneous nucleation mechanism. The incorporation of graphene did not change the nucleation mode essentially. In such growth mode, active sites on the electrode surface were activated simultaneously. Ni nuclei formed rapidly and grew slowly, which induced the formation of a uniform and dense coating structure [45].

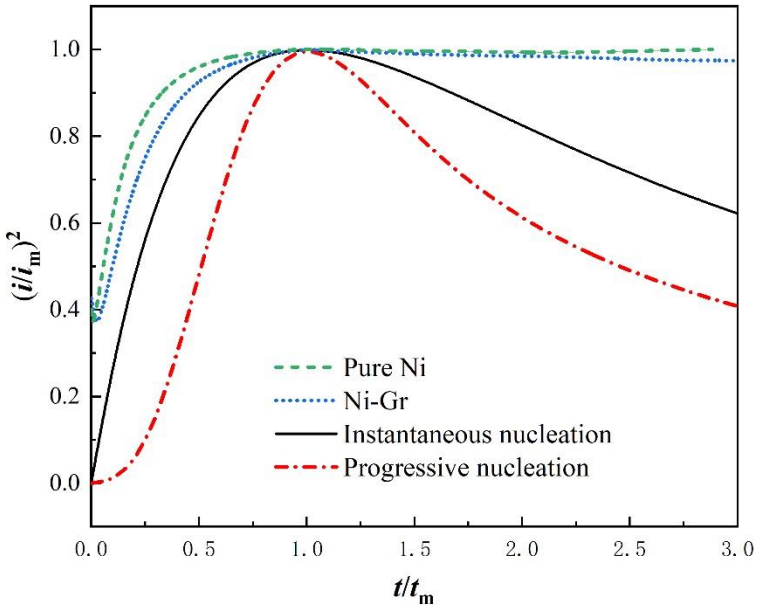

Figure 5. The non-dimensional curves of $(j/j_m)^2$ as a function of t/t_m of experimental transients in Fig. 4 at the deposition potential of −1.0 V compared to theoretical instantaneous and progressive nucleation curves.

Notably, there was a clear deviation between the experimental and theoretical curves, especially in the $t/t_m>1$ section. The establishment of the theoretical model followed the assumptions below: the electrode surface is smooth, the ion concentration of the plating solution remains unchanged, the crystal nucleus is treated as hemispherical microelectrodes, and the plane circle overlap method is adopted to deal with the overlap of three-dimensional crystal nuclei in the process of nucleation. However, the substrate surface was not absolutely smooth after polishing in the actual deposition process. The dislocations and defects on the surface provided a large number of active sites for the electrodeposition of Ni ions, which increased the electrochemical reaction area. Consequently, the reduction rate of current density with time was lower than the theoretical value. In addition, the actual deposition process was accompanied by concentration polarization, hydrogen evolution, and other side reactions. These resulted in the deviation between the theoretical and experimental curves.

Moreover, the nuclear number density (N) in the instantaneous nucleation mode can be calculated through Eq. (5):

$$N = 0.0652(\frac{8\pi cM}{\rho})^{-0.5}(\frac{nFc}{i_m t_m})^2 \quad (5)$$

where c is the bulk concentration of Ni^{2+}, M and ρ are the molar mass and density of the deposit, and nF is the molar charge of the electrodepositing species. Thus, the interrelationship of N, i_m, and t_m can be expressed as $N \propto (i_m t_m)^{-2}$. The nuclear number density ratio of pure Ni and Ni-Gr deposition is $N_{Ni\text{-}Gr}$:N_{Ni}=2.3:1, indicating that the graphene nanofillers facilitate a denser distribution of nuclei.

4.1.3 Morphology analysis

AFM morphologies of pure nickel and Ni-graphene deposits after 2 s, 5 s, and 30 s at the deposition potential of –1.0 V are shown in Fig. 6. The color scale at the same deposition time was kept the same for comparison. Once the constant potential was applied, a large number of nucleation sites were activated instantaneously, and the electrochemical reaction occurred driven by the overpotential. The metal deposits were distributed evenly and densely. The granular protrusions were small after 2 s deposition, and the grains exhibited hemispherical structure after 5 s deposition. When the deposition time was further prolonged to 30 s, the morphology gradually changed from epitaxial growth to fiber texture growth due to the convergence and overlapping of grains. A rice-shaped cluster structure dominated the coating surface, which was also observed in a previous study [46]. At the same time, secondary nucleation on the already formed granular sediment was not observed. Therefore, the nucleation mode of Ni and Ni-Gr depositions followed instantaneous nucleation, consistent with the results from chronoamperometry analysis.

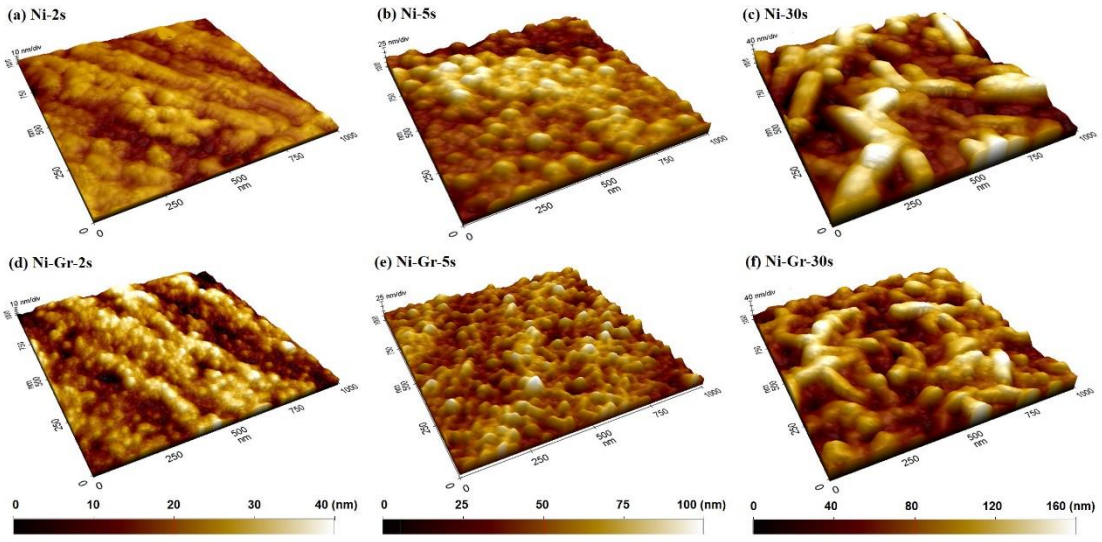

Figure 6. Three-dimensional AFM topography evolution of pure Ni and Ni-graphene coatings on mild steel at the deposition potential of −1.0 V.

To quantitatively compare the morphology evolution of the deposits, the main surface parameters were calculated according to ISO 25178-2: 2012, including root-mean-square height (S_q), skewness (S_{sk}), and kurtosis (S_{ku}). It can be seen from Table 6 that the S_q of the coating surface increased along with the deposition time, corresponding to the gradual formation of surface structures. S_{sk} and S_{ku} represent the symmetry and sharpness of the surface roughness structure, respectively. After deposition for 2 s, the value of S_{sk} was negative, indicating that the surface was dominated by valleys left by mechanical polishing. Moreover, S_{ku} was close to 3, suggesting that the rough structure was characterized by the co-existence of sharp and mild surface structures. When the deposition was carried out for 5 s, the positive S_{sk} indicated that the coating surface was dominated by peaks. The S_{ku} of pure Ni coating remained nearly the same, while that of Ni-graphene coating further increased. With the growth and aggregation of grains, rice-shaped grains replaced hemispherical grains after deposition for 30 s, and the values of S_{sk} and S_{ku} decreased.

Table 6. The surface parameters of pure Ni and Ni-graphene coatings on mild steel at the deposition potential of −1.0 V.

Coating type	Deposition time (s)	S_q (nm)	S_{sk} ($\times10^{-1}$)	S_{ku}
Pure Ni coating	2	6.05±1.07	–(5.20±0.59)	3.00±0.34
	5	13.03±1.56	3.62±1.15	2.96±0.12
	30	28.55±0.58	1.34±0.61	2.81±0.23
Ni-Gr composite coating	2	10.53±0.63	–(3.42±1.47)	3.06±0.07
	5	13.76±1.00	4.12±1.45	3.22±0.12
	30	28.25±0.25	1.97±0.07	2.82±0.25

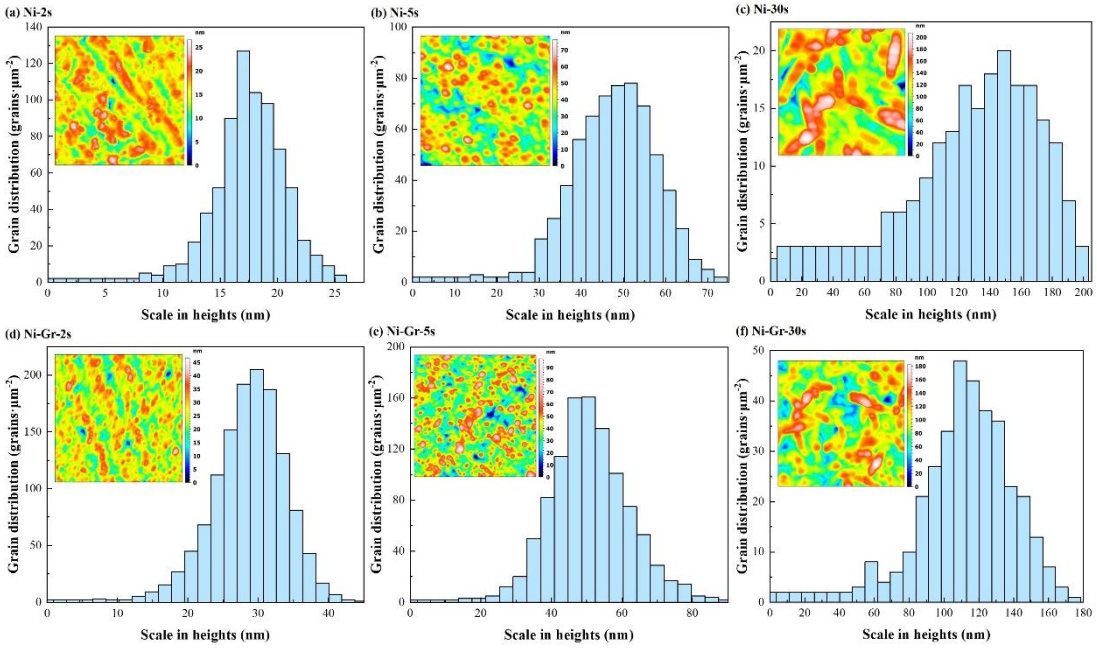

Figure 7. Peak count distribution histograms of (a-c) pure Ni coating and (d-f) Ni-graphene coating on mild steel at different deposition times.

To obtain better insight into the effect of graphene on coating morphology at the initial stage, the grain distribution of the peak structure was counted. The grain density of the composite coating was always apparently higher than that of the pure nickel coating, implying that the addition of graphene strongly impacted the grain size. The histogram and topography (inset) again validated the similar result obtained from chronoamperometry analysis that graphene addition can increase the nucleation density and refine the grain size.

4.2 Growth process of Ni-graphene composite coating

4.2.1 Co-deposition behavior

Fig. 8a illustrates the co-deposition process of Ni atom with graphene nanosheet, where solvent particles are hidden for better observation. The depositing atom was adsorbed on graphene nanosheet before the nucleation, due to the high specific surface area and surface activity of graphene. Moreover, graphene bent naturally due to the intrinsic flexibility of two-dimensional materials [10]. The shape diversity of graphene can evoke various unique properties, including electronic properties, chemical activities, functionalization affinity, energy storage capacity, etc. [47]. Thus, to adequately describe the configuration of graphene nanosheets in the coating matrix at the atomic level, it is necessary to consider the deformation of graphene nanosheets. Therefore, this work is closer to the actual situation than previous research that considered graphene as a rigid sheet [4].

The snapshots of Ni-graphene deposits at the early stage are shown in Fig. 8b-c. Focusing on the deposition behavior at the nanoscale, it can be seen that the atomic-level differences and defects on the polycrystalline substrate significantly impacted the deposition of atoms. In addition to the active sites on the surface of the polycrystalline substrate, the graphene reinforcing phase can also act as the nucleation site. Due to the ultra-large specific surface area and strong adsorption capacity of two-dimensional graphene, it can easily capture deposited atoms, leading to the selective deposition of nickel atoms on the surface and edge of graphene. The nickel atoms deposited on graphene promoted the three-dimensional island growth.

Many experimental studies reported texture alteration or grain reinforcement in graphene-reinforced coatings without discussing the role of graphene. Thus, particular attention was paid to the atom arrangement on the graphene-metal matrix interface herein. It can be seen from Fig. 8b-c that the Ni atom tended to adsorb on the hole site of graphene. The center spacing of planar graphene hexagon was 2.46 Å, while the spacing of close-packed nickel atoms was 2.49 Å. Although there was a certain degree of lattice mismatch between the lattice arrangement of nickel and graphene, a close-packed or defect-contained Ni atom plane can be formed on the honeycomb lattice of graphene. Graphene nanosheets existed on grain boundaries, which can disorder the matrix by retarding crystal growth along the original direction. Thus, the crystallographic orientation can be changed, and Ni grains were refined into a smaller size. Furthermore, the surface energy values of CVD-grown single-layered graphene and few-layered graphene are about 0.115 $J \cdot m^{-2}$ and 0.119 $J \cdot m^{-2}$ [48], respectively, while the surface energy of pure nickel measured at 0 K and melting point are 2.24 $J \cdot m^{-2}$ and 2.08 $J \cdot m^{-2}$, respectively [49, 50].

Therefore, the addition of graphene can break the long-range ordered structure of Ni and inhibit grain growth. The above experimental conclusions are consistent with the conclusion of this simulation.

In addition, when the graphene sheet was adsorbed with metal atoms, it spontaneously folds or bends, and a "brick-cement" structure was formed. It has been reported that this structure can effectively improve the compactness, impermeability, and wear resistance of the composite coating [51]. Furthermore, the abundant interplay between the graphene nanosheets and crystalline defects in the metal matrix leads to significant enhancement in the mechanical properties [52].

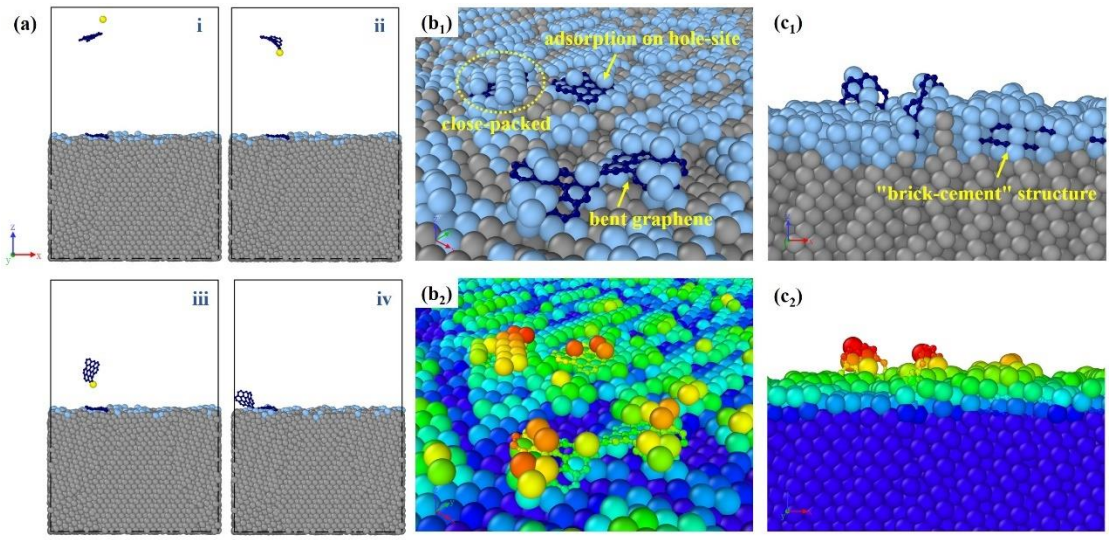

Figure 8. Co-deposition behavior of Ni atom and graphene nanosheet. (a) Adsorption between depositing Ni atom and graphene nanosheet, (b, c) preferential deposition of nickel atom on graphene nanosheets.

4.2.2 Effect of graphene on coating microstructure

Fig. 9 shows the morphology evolution of pure Ni deposit and Ni-graphene composite coating reinforced by 40 graphene flakes. The film morphology became gradually rougher with the deposition time, accompanied by the appearance of island structures and valleys. The root-mean-square surface roughness (R_q) can be calculated from the coordinates of surface atoms using Eq. (6-7),

$$R_q = \sqrt{\frac{1}{N}\sum_{i=1}^{N}(\bar{h} - h_i)^2} \quad (6)$$

$$\bar{h} = \frac{1}{N}\sum_{i=1}^{N} h_i \quad (7)$$

where N is the total number of surface atoms, h_i is the height of i^{th} surface atom, and $\bar{h}$ is the mean height. The surface roughness evolutions of pure Ni coating and Ni-graphene composite coating are plotted in Fig. 10. It can be found that the roughness of the coating gradually increased during the growth process, corresponding to the gradual formation of surface structure. The addition of graphene significantly increased the surface roughness, which was mainly triggered by the formation of sharp

protrusions. The incorporation of graphene increased the local thickness and provided active nucleation sites. Therefore, the deposited layer grew in an island mode.

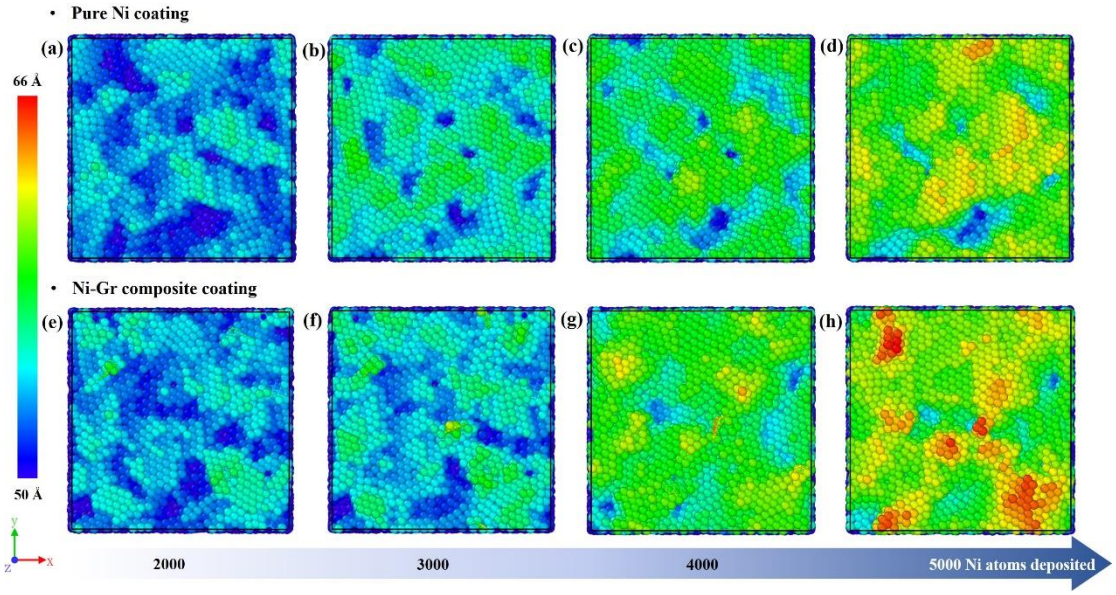

Figure 9. Effect of graphene incorporation on surface morphology. Surface morphology evolution of (a-d) pure Ni coating and (f-i) Ni-graphene composite coating.

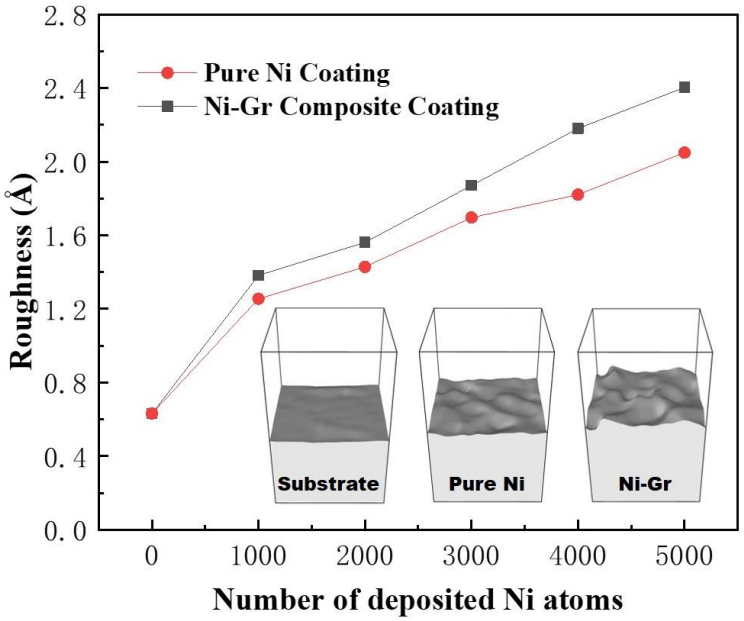

Figure 10. The evolution of coating surface roughness with the increase in number of deposited Ni atoms.

Experimentally, the composition of the plating solution can be directly adjusted, while it is difficult to control the embedding amount of graphene accurately. Besides, it is challenging to obtain the

distribution of graphene layers in the metal matrix. Thus, the effect of graphene on the coating microstructure was evaluated. As shown in Fig. 11, the surface roughness of the composite coatings showed a strong positive correlation with the graphene content. When graphene content was low, flakes were randomly distributed inside the coating. As previously analyzed, the embedding of graphene can increase the local thickness of the coating, resulting in the preferential deposition of Ni atoms. Thus, with the increase in graphene content, flakes formed complex structures within the coating matrix. To date, the precise control of lamellar nanofillers in the coating matrix remains a challenge [3]. When the embedding amount of graphene is too high, graphene tends to aggregate, which can cause crystal defects and result in the deterioration of the film quality [36]. The graphene dispersion inside the coating matrix also confirmed the existence of an optimal graphene content.

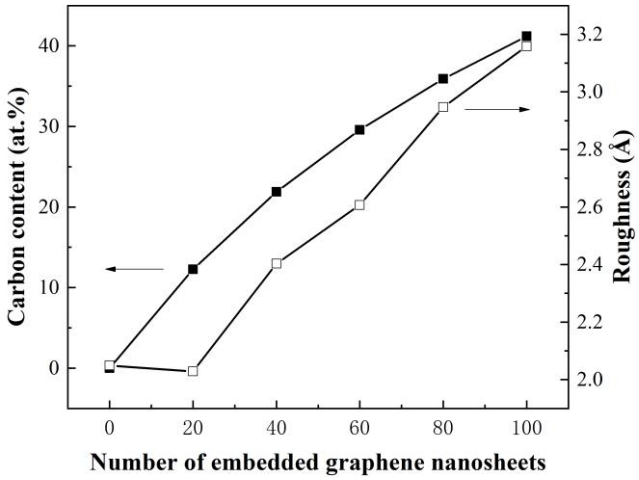

Figure 11. The roughness of Ni-graphene coatings with different graphene contents.

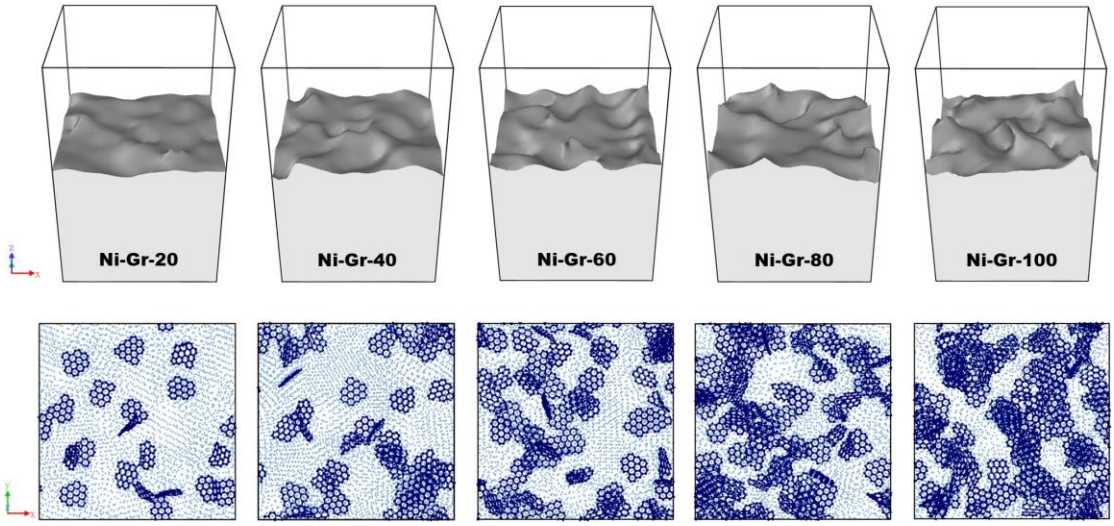

Figure 12. Contour plots and top-viewed graphene dispersion of Ni-graphene composite coatings with different graphene contents.

5. CONCLUSIONS

The growth process of Ni-graphene composite coating was investigated by combining electrochemical experiment, AFM observation, and MD simulation. This study provides a fundamental understanding of the Ni-graphene deposition mechanism, which is crucial for developing novel coatings with specific nanostructure or performance. The following conclusions can be drawn from this work:

(i) In the adopted plating solution, the addition of graphene induced a negative shift in the initial deposition potential. The enhanced cathodic polarization inhibited the reduction of nickel atoms, and the inhibition effect weakened with the increase in graphene concentration in the plating solution. Moreover, the addition of graphene led to the decrease in anodic peak current density, indicating that graphene improved the electrolytic corrosion resistance of the coating. However, when the concentration of graphene oxide in the plating solution was too high, the electrolytic corrosion resistance of the material decreased, indicating the existence of an optimal concentration of graphene oxide in the plating solution.

(ii) The electro-crystallization of pure Ni and Ni-graphene coatings followed the three-dimensional instantaneous nucleation mode under diffusion control. The addition of graphene increased peak current density and shortened nucleation relaxation time, which promoted the crystallization process of nickel on the electrode surface. Graphene nanosheets can provide nucleation sites for the deposition process, increase the nucleation density in the deposition process, and refine the grain size concurrently.

(iii) The established electrodeposition molecular dynamics model considered the flexible characteristics of graphene. The co-deposition behavior and the selective deposition of Ni atoms on the graphene layer were observed. In addition, the deposited nickel atoms tended to be adsorbed on the hole sites of graphene and formed a close-packed state, which can restrict the grain growth in the original orientation and induce grain refinement. The preferential deposition of Ni atoms can increase the local thickness of the coating and promote surface roughness. With the increase in graphene content, the root-mean-square roughness of the coating surface gradually increased from 2.049 Å (pure Ni coating) to 3.158 Å (Ni-graphene coating with a carbon content of 41.176 at.%).

CONFLICTS OF INTEREST
There are no conflicts to declare.

ACKNOWLEDGMENTS
This work is supported by the PetroChina Innovation Foundation (Grant No. 2019D-5007-0505), Fundamental Research Funds for the Central Universities (18CX05002A), Natural Science Foundation of Shandong Province (ZR2019MEE108), and Postgraduate Innovation Project of China University of Petroleum (No. YCX2021088).

References

1. F.C. Walsh, S. Wang, N. Zhou, *Curr. Opin. Electroche.*, 20 (2020) 8-19.
2. R. Zhang, G. Cui, X. Su, X. Yu, Z. Li, *J. Alloy. Compd.*, 829 (2020) 154495.
3. R. Zhang, X. Yu, Q. Yang, G. Cui, Z. Li, *Constr. Build. Mater.*, 294 (2021) 123613.
4. L. Zhang, Y. Zhu, N. Li, Y. Rong, H. Xia, H. Ma, *Appl. Surf. Sci.*, 433 (2018) 540-545.

5. H.E.M. Hussein, R.J. Maurer, H. Amari, J.J.P. Peters, L. Meng, R. Beanland, M.E. Newton, J.V. Macpherson, *ACS Nano*, 12(7) (2018) 7388-7396.
6. A. Radisic, F.M. Ross, P.C. Searson, *J. Phys. Chem. B*, 110(15) (2006) 7862-7868.
7. Z. Zeng, P. Barai, S.-Y. Lee, J. Yang, X. Zhang, W. Zheng, Y.-S. Liu, K.C. Bustillo, P. Ercius, J. Guo, Y. Cui, V. Srinivasan, H. Zheng, *Nano Energy*, 72 (2020) 104721.
8. T. Yoshioka, H. Matsushima, M. Ueda, *Electrochem. Commun.*, 92 (2018) 29-32.
9. O.M. Magnussen, *Chem–Eur. J.*, 25(56) (2019) 12865-12883.
10. J. Ding, H. Zhao, H. Yu, *Chem. Eng. J.*, 435 (2022) 134808.
11. X. Zhou, X. Liu, J. Lei, Q. Yang, *Comp. Mater. Sci.*, 172 (2020) 109342.
12. W.S. Hummers, R.E. Offeman, *J. Am. Chem. Soc.*, 80(6) (1958) 1339-1339.
13. A.K. Agegnehu, C.-J. Pan, J. Rick, J.-F. Lee, W.-N. Su, B.-J. Hwang, *J. Mater. Chem.*, 22(27) (2012) 13849-13854.
14. H. Zhang, N. Zhang, F. Fang, *Surf. Coat. Tech.*, 402 (2020) 126292.
15. S. Plimpton, *J. Comput. Phys.*, 117(1) (1995) 1-19.
16. LAMMPS Molecular Dynamics Simulator. Available from: http://lammps.sandia.gov.
17. A. Stukowski, *Model. Simul. Mater. Sc.*, 18(1) (2009) 015012.
18. OVITO. Available from: http://ovito.org/.
19. A. Brant, M. Sundaram, *Precis. Eng.*, 56 (2019) 412-421.
20. H. Zhang, N. Zhang, F. Fang, *Precis. Eng.*, 72 (2021) 122-143.
21. P. Hirel, *Comput. Phys. Commun.*, 197 (2015) 212-219.
22. J. Ustarroz, *Curr. Opin. Electroche.*, 19 (2020) 144-152.
23. Z. Zhang, M.G. Lagally, *Science*, 276(5311) (1997) 377.
24. V. Molinero, E.B. Moore, *J. Phys. Chem. B*, 113(13) (2009) 4008-4016.
25. B. Ghalami Choobar, H. Modarress, R. Halladj, S. Amjad-Iranagh, *Comp. Mater. Sci.*, 192 (2021) 110343.
26. B.-A. Mei, O. Munteshari, J. Lau, B. Dunn, L. Pilon, *J. Phys. Chem. C*, 122(1) (2018) 194-206.
27. T. Watanabe, Microstructure control theory of plated film, Nano-Plating Microstructure Control Theory of Plated Film and Data Base of Plated Film Microstructure, Elsevier, (2004) New York, USA.
28. G. Bonny, N. Castin, D. Terentyev, *Model. Simul. Mater. Sc.*, 21(8) (2013) 085004.
29. A. Arjhangmehr, S.A.H. Feghhi, *Comp. Mater. Sci.*, 151 (2018) 1-13.
30. X. Wu, H. Zhao, M. Zhong, H. Murakawa, M. Tsukamoto, Carbon, 66 (2014) 31-38.
31. S.J. Stuart, A.B. Tutein, J.A. Harrison, *J. Chem. Phys.*, 112(14) (2000) 6472-6486.
32. S. Inoue, Y. Matsumura, *Chem. Phys. Lett.*, 464(4) (2008) 160-165.
33. A. Montazeri, B. Panahi, *Appl. Surf. Sci.*, 457 (2018) 1072-1080.
34. Y. Hiwatari, Y. Kaneko, T. Mikami, K. Ohara, F. Asa, *Mol. Simulat.*, 33(1-2) (2007) 133-138.
35. T. Liang, M. Zhou, P. Zhang, P. Yuan, D. Yang, *Int. J. Heat Mass Tran.*, 151 (2020) 119395.
36. S. Li, G. Song, Y. Zhang, Q. Fu, C. Pan, *ACS Omega*, 6(21) (2021) 13728-13741.
37. R. Cui, Y. Han, Z. Zhu, B. Chen, Y. Ding, Q. Zhang, Q. Wang, G. Ma, F. Pei, Z. Ye, *J. Alloy. Compd.*, 777 (2019) 1159-1167.
38. X. Zhou, X. Yu, D. Jacobson, G.B. Thompson, *Appl. Surf. Sci.*, 469 (2019) 537-552.
39. A. Saraby-Reintjes, M. Fleischmann, *Electrochim. Acta*, 29(4) (1984) 557-566.
40. F. Hu, K.C. Chan, *Appl. Surf. Sci.*, 243(1) (2005) 251-258.
41. H. Zhang, N. Zhang, F. Fang, *Ultrason. Sonochem.*, 62 (2020) 104858.
42. K.S. Jyotheender, C. Srivastava, *Compos. Part B-Eng.*, 175 (2019) 107145.
43. C.-w. Su, F.-j. He, H. Ju, Y.-b. Zhang, E.-l. Wang, *Electrochim. Acta*, 54(26) (2009) 6257-6263.
44. B. Scharifker, G. Hills, *Electrochim. Acta*, 28(7) (1983) 879-889.
45. W. Tan, H. He, Y. Gao, Y. Peng, X. Dai, *J. Colloid Interf. Sci.*, 600 (2021) 492-502.
46. K. Asa Deepthi, R. Balachandran, B.H. Ong, K.B. Tan, H.Y. Wong, H.K. Yow, S. Srimala, *Appl. Surf. Sci.*, 360 (2016) 519-524.

47. S. Deng, V. Berry, *Mater. Today*, 19(4) (2016) 197-212.
48. C.D. van Engers, N.E.A. Cousens, V. Babenko, J. Britton, B. Zappone, N. Grobert, S. Perkin, *Nano Lett.*, 17(6) (2017) 3815-3821.
49. W.R. Tyson, W.A. Miller, *Surf. Sci.*, 62(1) (1977) 267-276.
50. P. Li, J. Liu, N. Nag, P.A. Crozier, *Surf. Sci.*, 600(3) (2006) 693-702.
51. J.H. Chu, L.B. Tong, M. Wen, Z.H. Jiang, D.N. Zou, S.F. Liu, H.J. Zhang, *Carbon*, 161 (2020) 577-589.
52. Z. Li, X. Fu, Q. Guo, L. Zhao, G. Fan, Z. Li, D.-B. Xiong, Y. Su, D. Zhang, *Int. J. Plasticity*, 111 (2018) 253-265.